Journal of Materials Chemistry C

ROYAL SOCIETY OF CHEMISTRY

PAPER

View Article Online
View Journal | View Issue

Cite this: J. Mater. Chem. C, 2024, 12, 3573

Metal co-doped cesium manganese chlorine nanocrystals with high efficiency and tunable red emission†

Shijia Liu,[a] Xuebin Zhang,[a] Qin Xu, *[a] Zhiheng Xu,[b] Haibo Zeng *[c] and Dandan Yang *[a]

Received 10th December 2023,
Accepted 30th January 2024

DOI: 10.1039/d3tc04539k

rsc.li/materials-c

Low photoluminescence efficiency and instability of lead-free halide perovskite nanomaterials are the main obstacles preventing their practical applications in the fields of optoelectronic devices and X-ray imaging. In this work, lanthanide-doped cesium manganese halide nanocrystals were synthesized by a simple hot injection method. The chemical composition and structural characteristics of the manganese-based perovskites were investigated in detail to prove that lanthanide ions successfully replaced partial manganese ions. As a result, red photoluminescence with a high photoluminescence quantum yield of 35% and a broad emission was obtained. More importantly, the roles of thulium and lead ions in enhancing the luminescence efficiency and tuning photoluminescence from 662 nm to 628 nm were studied in detail by modulating the molar ratios of thulium/lead. Furthermore, the thulium-doped NCs maintained a stable crystal phase and photoluminescence after two weeks. This work provides new insights into enhancing the photoluminescence and tuning the optical bandgap of a perovskite host with co-doping.

Introduction

In recent years, lead halide perovskite nanocrystals (NCs) have attracted much attention due to their outstanding optoelectronic properties, such as narrow emission linewidths,[1–3] tunable bandgap,[4,5] high photoluminescence quantum yield (PLQY)[6,7] and promising applications in photoelectric detectors,[8–10] light-emitting diodes (LEDs),[11,12] and X-ray imaging.[13,14] However, the toxicity and poor stability have hindered practical applications of lead halide perovskite NCs. To improve the chemical and photostability, a universal approach is to reduce the lead content by replacing Pb^{2+} ions with nontoxic and stable metal ions to form the lead-free or lead-less perovskite. For instance, Ge^{2+} or Sn^{2+}-based perovskites were synthesized by replacing Pb^{2+} with Ge^{2+} or Sn^{2+}. Unfortunately, the relatively low PLQY (<4%) and instability of these perovskites are still not satisfactory.[15] Cu-based perovskite NCs exhibit excellent optical properties;[16] however, they are easy to oxidize, resulting in a serious decline in optical properties. Huang *et. al.* demonstrated the solution-phase synthesis of cesium europium halide perovskite NCs but with PLQY a of only about 2%.[17] Outsides, other lead-free metal halides, such as Mn-based halides,[18] Cd-based halides,[19] and double perovskites, featured by self-trapped exciton (STE), large Stokes shift, large PL bandwidth, and long lifetimes, have been considered as alternatives for optoelectronic applications.[20] However, the synthesis of stable and highly efficient lead-free perovskite NCs is still a thorny issue.

Recently, color-tunable emission has been realized in Mn-based halides by changing the Mn^{2+} coordination structure, which has also received special attention.[21,22] In addition, Cs_3MnBr_5 NCs as crystal seeds were also used to synthesize $CsPbBr_3$ NCs with special morphology and dimensions.[23] Another noteworthy study is the improvement of optical properties and structural stability. For example, Guan *et al.* designed a low amount of Pb^{2+}-doped $CsMnCl_3$ NCs and improved the PLQY from 0.7% to 21% due to the effective energy transfer from $[PbCl_6]^{4-}$ to Mn^{2+} ions.[24] In contrast, the addition of Zn^{2+} ions serves as an obstacle to the energy transfer between Mn^{2+} ions, enhancing the PLQY of Zn^{2+}-doped $CsMnCl_3$ NCs with red emission at 654 nm from 56.3% to 77.1%.[25] In addition to the ion doping mentioned above, lanthanide ions (Ln^{3+}) can also

[a] Institute of Innovation Materials and Energy, School of Chemistry and Chemical Engineering, Yangzhou University, Yangzhou, 225002, China. E-mail: dandanyang@yzu.edu.cn
[b] Department of Nuclear Science and Technology, Nanjing University of Aeronautics and Astronautics, Nanjing 211106, China
[c] MIIT Key Laboratory of Advanced Display Materials and Devices, Institute of Optoelectronics & Nanomaterials, College of Materials Science and Engineering, Nanjing University of Science and Technology, Nanjing 210094, China

† Electronic supplementary information (ESI) available: Experimental part, Absorbance and PL spectra, XRD and HR-TEM, EDS mapping, XPS spectra. See DOI: https://doi.org/10.1039/d3tc04539k

promote luminescence conversion, but their progress as down-shifters is limited by the narrow absorption widths and very small absorption cross-section of Ln^{3+} ions.[26] For instance, $CsMnBr_3$ NCs as an efficient sensitizer to transfer energy to Ln^{3+} ions, resulted in the decrease of Mn^{2+} red emission and generated vaying NIR emissions.[26,27] However, during the emission by Ln^{3+}-doped perovskite NCs, the PL efficiency of excitons emitted by the perovskite host increases, which has not attracted enough attention. Therefore, the selection and design of metal co-doping ions play an important role in exploring the PL properties of lead-free perovskites.

In this work, we prepared lanthanide-doped $CsMnCl_3$ NCs with red emission at 662 nm by a hot injection method. Structure, composition, and chemical state studies confirmed that Ln^{3+} ions partially replaced Mn^{2+} ions, which were successfully introduced into $CsMnCl_3$ NCs. As a result, the PL intensity is monotonously enhanced with the increase in the concentration of Ln^{3+} doping (7% Tm^{3+}, 13% Yb^{3+}, and 7% Er^{3+}), and the highest PLQY of up to 35% was obtained for Ln^{3+}-$CsMnCl_3$ NCs. To further study the role of Ln^{3+} ions in enhancing the luminescence of $CsMnCl_3$ NCs and optimizing their optical properties, the Pb/Tm co-doped $CsMnCl_3$ NCs were synthesized. The energy levels of Tm^{3+} ions play a transitional role in the process of exciton transfer from the Pb^{2+} to the $CsMnCl_3$ host, resulting in improving the PL efficiency of the $CsMnCl_3$ host. Furthermore, modulating the Pb doping concentration can break the spin-forbidden transition of Pb/Tm co-doped $CsMnCl_3$ NCs, resulting in tunable photoluminescence from 662 nm to 628 nm, and the highest PLQY of up to 52.2% was obtained. In addition, the good stability of Tm^{3+}-$CsMnCl_3$ NCs compared to $CsMnCl_3$ NCs is discussed.

The synthesis process of colloidal $CsMnCl_3$ and Ln^{3+}-$CsMnCl_3$ NCs is similar to the one used to prepare lead-based perovskite NCs by a simple hot-injection method (see the detailed Experimental section in the ESI,† S1). It is slightly different from our approach and the effects of different solvents on the solubility and luminescence of $CsMnCl_3$ NCs are discussed. Four common solvents, including toluene, cyclohexane, *n*-hexane, octane, and tetradecane, were used to dissolve $CsMnCl_3$ NCs and maintain their quality. Surprisingly, the octane solution of $CsMnCl_3$ NCs maintained good solubility and strong fluorescence, whereas the NCs with strong luminescence in tetradecane solution showed serious agglomeration and the shape evolved from the hexagonal to rod structure (Fig. S2, ESI†), which may be related to the chain length of alkanes and intermolecular forces (Fig. S3, ESI†).[28] In order to balance the luminescence and dispersion, octane is the best choice for $CsMnCl_3$ NCs.

Fig. 1a exhibits the crystal structure of $CsMnCl_3$ along an axis. $CsMnCl_3$ NCs have a hexagonal structure formed by Mn_3Cl_{12} chains (three face-sharing $[MnCl_6]^{4-}$ octahedral unit) shared by corners and stabilized by cesium ions ($R\bar{3}m$ space group). Taking Tm as an example, Tm^{3+} ions are doped to form $[TmCl_6]^{4-}$octahedron to substitute $[MnCl_6]^{4-}$, in principle, generating a cation vacancy (V_{Mn}).[26] After doping with Tm^{3+} ions, a light pink transparent solution emits stronger red light

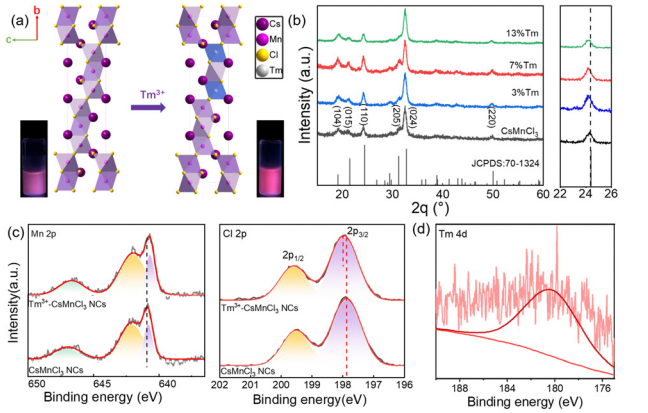

Fig. 1 (a) Schematic diagram of the structure of the undoped and Tm^{3+}-doped $CsMnCl_3$ NCs. The insets show the comparative photos of red emission under a 365 nm UV lamp. (b) XRD patterns (left panel) and magnified XRD peaks (right panel) of $CsMnCl_3$ and Tm^{3+}-$CsMnCl_3$ NCs. The XPS data of (c) Mn 2p and Cl 2p for Tm^{3+}-$CsMnCl_3$, and $CsMnCl_3$ NCs, (d) Tm 4d for Tm^{3+}-$CsMnCl_3$ NCs.

under a 365 nm UV lamp, as shown in the illustration of Fig. 1a. Fig. 1b presents a series of X-ray diffraction (XRD) patterns of Tm^{3+}-$CsMnCl_3$ NCs ($CsMnCl_3$ NCs with different Tm^{3+} doping concentrations), and all diffraction peaks correspond well to the standard diffractions from hexagonal $CsMnCl_3$ NCs (PDF card 70-1324). After partial substitution of Mn^{2+} (0.67–0.83 Å, depending on the high- or low-spin coordination) by the larger Tm^{3+} (0.87 Å), the (110) diffraction peak gradually shifts to a smaller angle (from 24.4° to 24.2°) (Fig. 1b, right panel).[25,29] This can be explained by the expansion of the crystal lattice after the incorporation of Tm^{3+}, which in turn proves that Tm^{3+} ions were successfully introduced into the $CsMnCl_3$ lattice without altering the structure.

To confirm the chemical composition and electronic characteristics of Mn, Cl, and Tm elements in $CsMnCl_3$ and Tm^{3+}-$CsMnCl_3$ NCs, X-ray photoelectron spectroscopy (XPS) measurements were performed. Fig. 1c shows the chemical states of the two samples of Mn and Cl. The main peaks in the Mn 2p XPS spectrum at 640.85 eV and 642.09 eV correspond to $2p_{3/2}$ and $2p_{1/2}$, respectively, as well as a satellite peak at around 646.9 eV, indicating the +2 valence state of Mn.[27] Clear changes can be seen with the movement to low binding energy compared to that with $CsMnCl_3$ NCs, which contribute to the fact that the electron absorption capacity of Tm is less than that of Mn, and increases the electron cloud density around Mn and shifts it to the low binding energy. In contrast, the peaks of Cl 2p shift slightly in the direction of high binding energy after Tm doping, indicating the interaction between Tm and Cl ions. In addition, Fig. 1d shows that the weak binding energy located at 178.9 eV of Tm 2p is due to a small amount of Tm doping, indicating that the Tm^{3+} ions were doped into $CsMnCl_3$ NCs. The movement of Cs 3d (Fig. S4, ESI†) is not obvious, demonstrating that the incorporation of Tm^{3+} into the host lattice Mn^{2+}, rather than that of Cs^+ and Cl^-.

Fig. S5 (ESI†) shows the transmission electron microscopy (TEM) images of $CsMnCl_3$ NCs with different $TmCl_3$ contents.

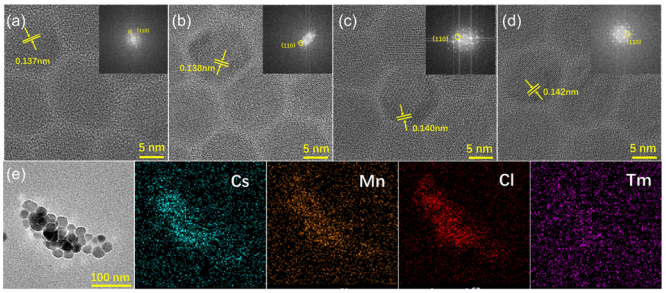

Fig. 2 (a)–(d) HR-TEM images and corresponding FFT pattern of 0%, 3%, 7%, and 13% Tm doping of $CsMnCl_3$ NCs. (e) TEM and EDS mapping images of Tm^{3+}-$CsMnCl_3$ NCs.

All samples exhibited good monodispersity and homogeneous hexagonal shapes. Meanwhile, the average lengths are 14.35 nm, 16.89 nm, 18.16 nm, and 18.80 nm, respectively. Obviously, the size of pure hexagonal-doped NCs increases with the increase in the content of Tm^{3+} doping, which may be attributed to the partial substitution of Tm^{3+} ions with (0.87 Å) to Mn^{2+} (0.67–0.83 Å). Similar results have been reported for the hexagonal $CsCdBr_3$ NCs.[30] To further prove the effect of Tm^{3+} doping on the structure of $CsMnCl_3$ NCs, high-resolution TEM (HR-TEM) images of $CsMnCl_3$ NCs with different Tm^{3+} doping contents were conducted, as shown in Fig. 2a–d. With the increases of Tm^{3+} ions, the crystal plane spacing of $CsMnCl_3$ increases continuously from 0.137 to 0.142 nm, which indicates that the Mn^{2+} ions are partially substituted by Tm^{3+} ions with larger ionic radii, leading to a slight lattice expansion. This result is consistent with the XRD variations (Fig. 1b). To confirm the existence of Tm^{3+} ions in $CsMnCl_3$ NCs, energy dispersion spectroscopy (EDS) measurements of Tm^{3+}-$CsMnCl_3$ NCs were conducted, as shown in Fig. 2e. It can be seen from the EDS data that Cs, Mn, Cl, and Tm elements were uniformly distributed in these nanocrystals, and the Tm element was distributed scarcely compared to the other elements. Based on the above results, a small amount of Tm^{3+} ions can be doped into the $CsMnCl_3$ lattice, partially replacing the Mn^{2+} ions, and no new morphology appeared.

Fig. 3a and b show a comparison of the absorption spectra and PL excitation (PLE) spectra of $CsMnCl_3$ and Tm^{3+}-$CsMnCl_3$ NCs, respectively. The materials showed similar peaks with five structured peaks at 355 nm, 374 nm, 420 nm, 448 nm, and 540 nm, which are ascribed to the electronic transition of Mn^{2+} ions from $^6A_1(S)$ to $^4T_1(P)$, $^4E(D)$, $^4T_2(D)$, $^4A1/^4E(G)$, and $^4T_2(G)$, respectively.[31] These peaks typically come from the d–d transitions in the octahedrally coordinated Mn^{2+} ions. The assignment of Mn^{2+} based on the d–d transitions has been studied in detail.[20,32] Fig. 3c presents the PL spectra of $CsMnCl_3$ NCs under 420 nm excitation, and the impact of Tm^{3+} doping on their luminescence properties was studied. For the undoped sample, there is a PL peak at 662 nm, while for Tm^{3+}-$CsMnCl_3$ NCs, the red emission intensity initially increases and then decreases with the increase of the Tm^{3+} doping contents, among which, the PL intensity of 7% doped material was the highest and the peak position remained unchanged, which coincided with the luminescence under the ultraviolet lamp

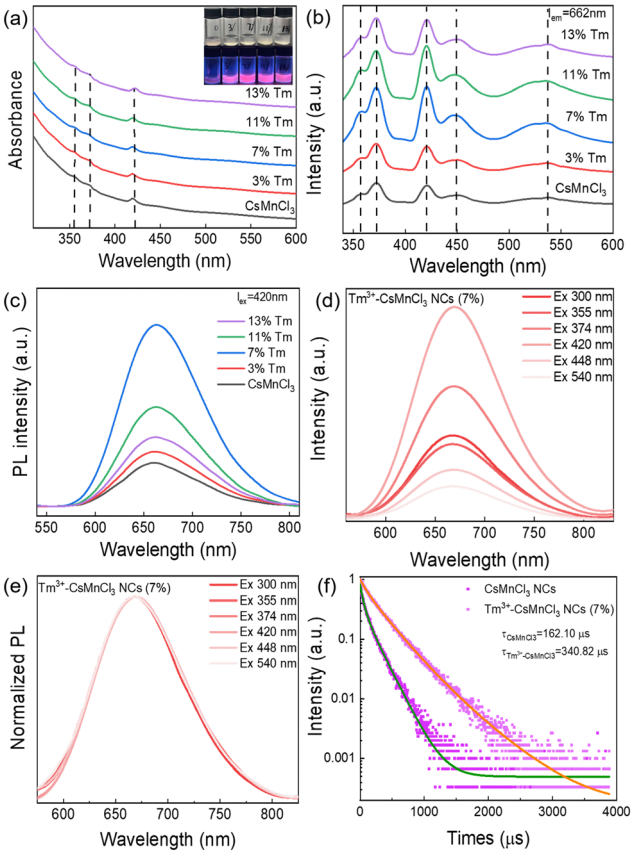

Fig. 3 (a)–(c) UV-VIS, PLE (λ_{em} = 662 nm, range: 340–600 nm) and PL (λ_{ex} = 420 nm, range: 540–810 nm) spectra of $CsMnCl_3$ and Tm^{3+}-$CsMnCl_3$ NCs. (d) and (e) PL and normalized PL emission spectra of 7% Tm^{3+}-$CsMnCl_3$ NCs after illuminations at the six different excitation wavelengths. (f) PL decay curves (λ_{ex} = 365 nm, λ_{em} = 662 nm) of $CsMnCl_3$ NCs with 7% Tm^{3+} doping.

(the illustration in Fig. 3a). In addition, we studied the PL emission spectra at different excitation wavelengths selected from the absorption spectra of the undoped and 7% Tm^{3+}-$CsMnCl_3$ NCs, as well as the excitation wavelength at 300 nm and found that 7% Tm^{3+}-$CsMnCl_3$ NCs have the same emission peak at 662 nm, identical spectral shape, and FWHM (Fig. 3d and e). Thus, the red PL emission is attributed to the relaxation from the low energy excited state to the ground state of Mn^{2+} (from $^4T_1$ to $^6A_1$), as illustrated in Fig. 4, which is consistent with the assignment of the red emission in the octahedrally coordinated Mn^{2+}. However, for $CsMnCl_3$ NCs, the PL emission spectra show a little change at the six different excitation wavelengths (Fig. S6a, ESI† and Fig. 6b), which may be related to the defect state. Fig. 3f shows that the 662 nm emission band of the undoped and 7% Tm^{3+}-$CsMnCl_3$ NCs has an average lifetime of 162.10 μs and 340.82 μs after fitting with triple exponential decay, respectively. The relatively short lifetime of $CsMnCl_3$ NCs indicates that the non-radiative recombination is dominant, which results in a low PLQY of 0.3%.[22] In contrast, the 7% Tm^{3+}-doped $CsMnCl_3$ NCs were diluted to a certain concentration, and the measured PLQY was 35%. In addition, we attempted doping with other lanthanide dopants, such as

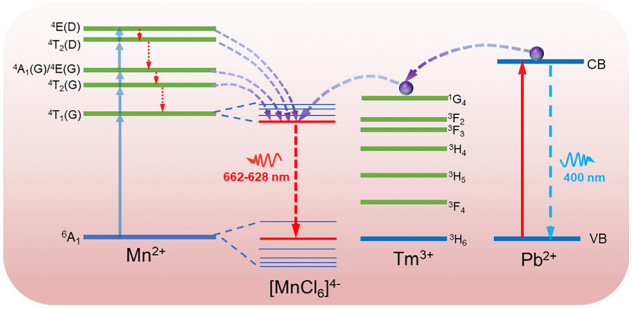

Fig. 4 The schematic diagram for the emission mechanism of undoped and Pb/Tm co-doped $CsMnCl_3$ NCs.

Yb^{3+} and Er^{3+} ions. Fig. S7 (ESI†) shows that the PL intensity at 662 nm for the sample with 13% Yb is the strongest, while the PL intensity at 662 nm for the sample with 7% Er^{3+} was the highest. The enhanced luminescence of Ln^{3+}-$CsMnCl_3$ NCs may be due to the partial substitution of Ln^{3+} ions for Mn^{2+} ions, which effectively suppresses the energy transfer between Mn^{2+} and promotes the excitons to be confined to the $[MnCl_6]^{4-}$ octahedron (Fig. 4). However, the high doping content of Ln^{3+} will lead to the concentration quenching effect due to the non-radiative energy transfer between the dopant and lattice.

To gain more insights into the role of Ln^{3+} ions in enhancing the luminescence of $CsMnCl_3$ NCs and optimizing their optical properties, Pb/Tm co-doped $CsMnCl_3$ NCs were prepared by the introduction of a small amount of Pb^{2+} ions. The Pb-doped $CsMnCl_3$ NCs were used as a reference sample, Fig. 5a shows that the absorption around 283 nm was greatly enhanced due to the parity allowed transition from $^1S_0$ to $^3P_1$ of $[PbCl_6]^{4-}$ octahedrons.[24,33] Tm was selected as the $^1G_4$ energy level, which is the most perfect candidate for the formation of the gradient

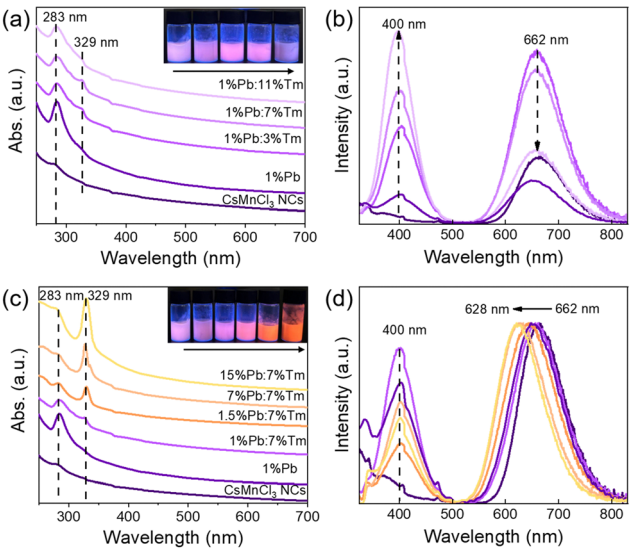

Fig. 5 (a) UV-vis and (b) PL spectra of $CsMnCl_3$ NCs and Pb/Tm co-doped $CsMnCl_3$ NCs with changing Tm doping contents. (c) UV-vis and (d) PL spectra of $CsMnCl_3$ NCs and Pb/Tm co-doped $CsMnCl_3$ NCs by changing the Pb doping contents. The insets are the luminescence photographs of the above samples under daylight and a 365 nm UV lamp.

levels.[34] With the increases in the doping content of Tm, the absorption peak at 283 nm decreased, and the emission spectra for Pb/Tm co-doped NCs revealed the presence of $CsMnCl_3$ host and intrinsic Pb^{2+} ions (Fig. 5b). As the Tm^{3+} doping concentration increases to 3–7%, more excitons are transferred to the $CsMnCl_3$ host and then released, accompanied by the emission of more photons. As a result, the PL intensity of the $CsMnCl_3$ host increases significantly. The strong peak at 662 nm is mainly attributed to the emission of the $CsMnCl_3$ host. These results show that a part of photoinduced exciton will be transferred from the Pb^{2+} host to the $^1G_4$ energy level of Tm^{3+}, and then these excitons will be transferred downward to the lower energy state $^4T_1$ of Mn^{2+}, promoting more excitons to be confined to the $[MnCl_6]^{4-}$ octahedron. Finally, the exciton will be released with the emission spectra of 662–628 nm (Fig. 4). Thus, Tm^{3+} ions play a transitional role in the process of exciton transfer, making it easier and more efficient to transfer excitons from the Pb^{2+} host to the $CsMnCl_3$ host. Interestingly, the PL intensity decreases with higher Tm doping contents, accompanied by a significant increase for the PL peak at 400 nm. The strong emission at 400 nm mainly belongs to the emission of intrinsic Pb^{2+} ions due to the non-radiative energy transfer between the Tm^{3+} dopant and the lattice.

To verify the role of Pb^{2+} ions, we further investigated the effect of Pb doping content on the optical properties of $CsMnCl_3$ NCs. Both 7% Tm^{3+}-doped and 1%Pb/7%Tm co-doped exhibited excellent optical properties, and found that they have an obvious absorption peak at 329 nm compared with the other samples; the NCs with 7% Tm^{3+} acted as a reference sample. Interestingly, when the Pb doping concentration increased from 1% to 15%, the absorption peak at 329 nm was significantly enhanced (Fig. 5c), which is attributed to the spin-forbidden $^4T_1(P)$ to $^6A_1(S)$ transition. The presence of an obvious absorption peak in Pb/Tm co-doped $CsMnCl_3$ NCs implies that the spin-forbidden transition is further broken depending on the doping, leading to lower crystal symmetry.[35,36] Correspondingly, the absorption peak at 283 nm gradually weakens. Hence, the tunable PL of Pb/Tm co-doped $CsMnCl_3$ NCs may mainly be dependent on the broken spin-forbidden transition. Thus, Fig. 5d shows that the red emission showed a blue shift from 662 nm to 628 nm, which originated from the d–d transitions in the $[MnCl_6]^{4-}$ octahedron rather than an isolated Mn^{2+} ion, and the emission peak at 400 nm remained unchanged. Moreover, the PL peak remained unchanged for $CsMnCl_3$ NCs with Pb doping from 7% to 15%.

Fig. S8 (ESI†) is the Tauc plot curve converted by the Kubelka–Munk equation for the bandgap calculation. The bandgap of $CsMnCl_3$ NCs is estimated to be 3.85 eV, which is consistent with that from a previous report.[24] As the Pb/Tm doping ratio increases, the corresponding bandgap decreases sequentially. The band gap decreased to 3.39 eV when the doping of Pb was 15%. In addition, the optimum PLQY of the PL peak at 628 nm is 52.5%. Correspondingly, the PL decay lifetime of Pb/Tm co-doped $CsMnCl_3$ NCs with the emission peak at 628 nm can be fitted with triple-exponential decay, and an average lifetime of 333.93 μs was obtained (Fig. S9, ESI†),

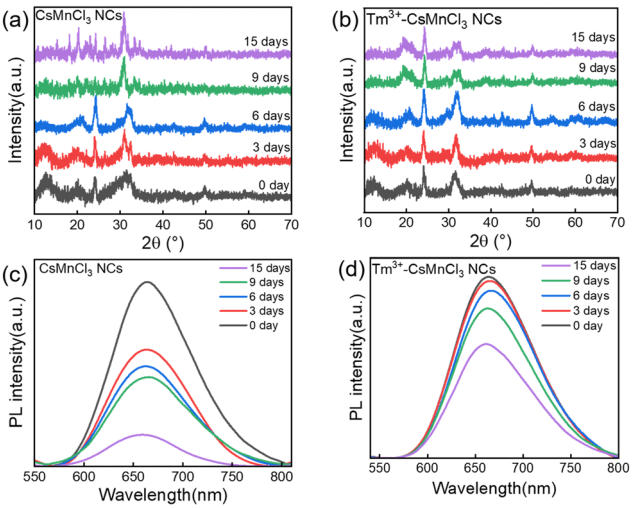

Fig. 6 Time-dependent XRD patterns of (a) $CsMnCl_3$ and (b) Tm^{3+}-$CsMnCl_3$ NCs. PL variation of (c) $CsMnCl_3$ and (d) Tm^{3+}-$CsMnCl_3$ NCs after different storage times.

which is similar to that of 7% Tm^{3+}-$CsMnCl_3$ NCs (340.82 μs). Table S1 (ESI†) summarizes in detail the parameters of PL decay lifetimes of the undoped, 7% Tm^{3+}, and Pb/Tm co-doped $CsMnCl_3$ NCs. Therefore, Pb^{2+} ions cannot play a similar effect as Tm^{3+} ions, and Pb^{2+} ions mainly regulate the PL emission of $CsMnCl_3$ NCs due to the absence of the forbidden transition. When the Pb content increased to 50%, the absorption peak at 328 nm gradually disappeared, as shown in Fig. S10 (ESI†), and a new absorption peak at 384 nm appeared. As a result, the PL spectra of the Pb/Tm co-doped NCs show the yellow-orange emission at 606 nm and ultraviolet emission at 400 nm, which results from the isolated Mn^{2+} ions and $CsPbCl_3$ NCs.[37] The XRD pattern well corresponds to the cubic phase of $CsPbCl_3$ NCs (Fig. S11, ESI†), indicating the formation of the $CsPbCl_3$ host. Based on the above results, the tunable red emission of Tm^{3+}-$CsMnCl_3$ NCs with partial Pb doping breaks through the limitation of a single-emission peak of $CsMnCl_3$ NCs, and Pb/Tm co-doped $CsMnCl_3$ NCs with high efficiency are further realized.

The phase and storage stability of undoped and Tm^{3+}-doped $CsMnCl_3$ NCs were tested at 50% humidity and 25 °C under atmospheric pressure. Fig. 6a and b show the XRD patterns and PL spectra of the two thin film samples, the Tm^{3+}-doped NCs with red emission maintained the hexagonal phase after two weeks, while undoped NCs were transferred from the red-emitting hexagonal phase to the blue emitting hexagonal $Cs_2MnCl_4(H_{20})_2$ phase, and partially decomposed into CsCl and $MnCl_2$ after one week (Fig. S12, ESI†). In addition, as the storage time increases, the Tm^{3+}-doped NCs and undoped NCs maintained 63% and 17% of their PL intensities recorded at room temperature after two weeks (Fig. 6c and d).

Conclusions

In summary, we successfully developed various lanthanide-doped $CsMnCl_3$ NCs *via* the hot-injection method and expanded the optical properties of the perovskite NCs. The substitution of Ln^{3+} ions for Mn^{2+} ions into the internal lattice of $CsMnCl_3$ NCs was preliminarily demonstrated by XRD, TEM, and EDX measurements. Interestingly, the introduction of Ln^{3+} ions considerably improved the red emission centered at 662 nm for $CsMnCl_3$ NCs. PLQY was successfully enhanced from 0.3% to 35%. In addition, the Pb/Tm co-doped $CsMnCl_3$ NCs were synthesized, the energy levels of Tm^{3+} ions played a transitional role in the process of exciton transfer from the Pb^{2+} to the $CsMnCl_3$ host while controlling the amount of Pb doping to obtain tunable PL emission from 662 nm to 628 nm due to the absence of the forbidden transition, and the PLQY was further optimized to 52.5%. Moreover, Tm^{3+}-$CsMnCl_3$ NCs maintained good phase and storage stability compared with undoped NCs after two weeks. We believe that this work provides a new approach to improving the PL properties, tuning the optical bandgap, and exploring the luminescent mechanism for lead-free perovskite NCs.

Author contributions

D. Yang and Q. Xu supervised the study. D. Yang conceived the idea for the manuscript and designed the experiments. S. Liu and X. Zhang carried out the synthesis and characterizations of NCs. The manuscript was mainly written by D. Yang and S. Liu. Z. Xu, and H. Zeng revised and improved the manuscript. All authors discussed the results and commented on the manuscript.

Conflicts of interest

There are no conflicts to declare.

Acknowledgements

This work was financially supported by the National Natural Science Foundation of China (62204215 and 12275132), the Basic Science (Natural Science) Research Project of Colleges and Universities in Jiangsu Province (22KJB430012), and China Postdoctoral Science Foundation (2023M742946). Yangzhou University Testing Center was also thanked for the XPS and XRD characterizations.

Notes and references

1 D. Zhang, Y. Yang, Y. Bekenstein, Y. Yu, N. A. Gibson, A. B. Wong, S. W. Eaton, N. Kornienko, Q. Kong, M. Lai, A. P. Alivisatos, S. R. Leone and P. Yang, *J. Am. Chem. Soc.*, 2016, **138**, 7236–7239.
2 S. Wei, Y. Yang, X. Kang, L. Wang, L. Huang and D. Pan, *Chem. Commun.*, 2016, **52**, 7265–7268.
3 Y. Tong, E. Bladt, M. F. Ayguler, A. Manzi, K. Z. Milowska, V. A. Hintermayr, P. Docampo, S. Bals, A. S. Urban, L. Polavarapu and J. Feldmann, *Angew. Chem., Int. Ed.*, 2016, **55**, 13887–13892.

4 X. Zhu, S. Meng, Y. Zhao, S. Zhang, J. Zhang, C. Yin and S. Ye, *J. Phys. Chem. Lett.*, 2020, **11**, 9587–9595.
5 C. Jang, K. Kim, H. W. Nho, S. M. Lee, H. Mubarok, J. H. Han, H. Kim, D. Lee, Y. Jang, M. H. Lee, O. H. Kwon, S. K. Kwak, W. B. Im, M. H. Song and J. Park, *Small*, 2023, **19**, 2206668.
6 J. N. Yang, Y. Song, J. S. Yao, K. H. Wang, J. J. Wang, B. S. Zhu, M. M. Yao, S. U. Rahman, Y. F. Lan, F. J. Fan and H. B. Yao, *J. Am. Chem. Soc.*, 2020, **142**, 2956–2967.
7 F. Liu, Y. Zhang, C. Ding, S. Kobayashi, T. Izuishi, N. Nakazawa, T. Toyoda, T. Ohta, S. Hayase, T. Minemoto, K. Yoshino, S. Dai and Q. Shen, *ACS Nano*, 2017, **11**, 10373–10383.
8 T. Yang, Y. Zheng, Z. Du, W. Liu, Z. Yang, F. Gao, L. Wang, K. C. Chou, X. Hou and W. Yang, *ACS Nano*, 2018, **12**, 1611–1617.
9 Y.-Z. Shen, J. Guan, C. Ma, Y. Shu, Q. Xu and X.-Y. Hu, *Anal. Chem.*, 2022, **94**, 1742–1751.
10 Y. Shu, Q. Ye, T. Dai, J. Guan, Z. Ji, Q. Xu and X. Hu, *J. Hazard. Mater.*, 2022, **430**, 128360.
11 S. Zhang, H. Liu, X. Li and S. Wang, *Nano Energy*, 2020, **77**, 105302.
12 J. Guan, M. Song, L. Chen, Y. Shu, D. Jin, G. Fan, Q. Xu and X.-Y. Hu, *Carbon*, 2021, **175**, 93–100.
13 L. Wang, K. Fu, R. Sun, H. Lian, X. Hu and Y. Zhang, *Nano-Micro Lett.*, 2019, **11**, 52.
14 J.-X. Wang, O. M. Bakr and O. F. Mohammed, *Matter*, 2022, **5**, 2547–2549.
15 D. Yang, X. Zhang, S. Liu, Z. Xu, Y. Yang, X. Li, Q. Ye, Q. Xu and H. Zeng, *Nanoscale*, 2023, **15**, 1637–1644.
16 S. Liu, H. Liu, G. Zhou, X. Li and S. Wang, *Chem. Eng. J.*, 2022, **427**, 1314430.
17 J. Huang, T. Lei, M. Siron, Y. Zhang, S. Yu, F. Seeler, A. Dehestani, L. N. Quan, K. Schierle-Arndt and P. Yang, *Nano Lett.*, 2020, **20**, 3734–3739.
18 T. Chang, Y. Dai, Q. Wei, X. Xu, S. Cao, B. Zou, Q. Zhang and R. Zeng, *ACS Appl. Mater. Interfaces*, 2023, **15**, 5487–5494.
19 X. Zhou, K. Han, Y. Wang, J. Jin, S. Jiang, Q. Zhang and Z. Xia, *Adv. Mater.*, 2023, **35**, 2212022.
20 A. M. Anthony, M. K. Pandian, P. Pandurangan and M. Bhagavathiachari, *ACS Appl. Mater. Interfaces*, 2022, **14**, 29735–29743.
21 K. Li, W. Zhang, L. Niu, Y. Ye, J. Ren and C. Liu, *Adv. Sci.*, 2022, **10**(4), 2204843.
22 Q. Kong, B. Yang, J. Chen, R. Zhang, S. Liu, D. Zheng, H. Zhang, Q. Liu, Y. Wang and K. Han, *Angew. Chem., Int. Ed.*, 2021, **60**, 19653–19659.
23 S. Bera, S. Banerjee, R. Das and N. Pradhan, *J. Am. Chem. Soc.*, 2022, **144**, 7430–7440.
24 L. Q. Guan, S. Shi, X. W. Niu, S. C. Guo, J. Zhao, T. M. Ji, H. Dong, F. Y. Jia, J. W. Xiao, L. D. Sun and C. H. Yan, *Adv. Sci.*, 2022, **9**, 2201354.
25 X. Hao, H. Liu, W. Ding, F. Zhang, X. Li and S. Wang, *J. Phys. Chem. Lett.*, 2022, **13**, 4688–4694.
26 H. Bahmani Jalali, A. Pianetti, J. Zito, M. Imran, M. Campolucci, Y. P. Ivanov, F. Locardi, I. Infante, G. Divitini, S. Brovelli, L. Manna and F. Di Stasio, *ACS Energy Lett.*, 2022, **7**, 1850–1858.
27 Y. Su, L. Yuan, B. Wang, S. Wu and Y. Jin, *J. Colloid Interface Sci.*, 2022, **624**, 725–733.
28 J. Zhao, G. Pan, W. Xu, S. Jin, H. Zhang, H. Gao, M. Kang and Y. Mao, *Chem. Commun.*, 2020, **56**, 14609–14612.
29 E. Song, Z. Chen, M. Wu, S. Ding, S. Ye, S. Zhou and Q. Zhang, *Adv. Opt. Mater.*, 2016, **4**, 798–806.
30 J. Guo, Q. Hu, M. Lu, A. Li, X. Zhang, R. Sheng, P. Chen, Y. Zhang, J. Wu, Y. Fu, G. Sun, W. W. Yu and X. Bai, *Chem. Eng. J.*, 2022, **427**, 131010.
31 H. Xiao, P. Dang, X. Yun, G. Li, Y. Wei, Y. Wei, X. Xiao, Y. Zhao, M. S. Molokeev, Z. Cheng and J. Lin, *Angew. Chem., Int. Ed.*, 2020, **60**, 3699–3707.
32 J. Almutlaq, W. J. Mir, L. Gutiérrez-Arzaluz, J. Yin, S. Vasylevskyi, P. Maity, J. Liu, R. Naphade, O. F. Mohammed and O. M. Bakr, *ACS Mater. Lett.*, 2021, **3**, 290–297.
33 W. Zhang, J. Wei, Z. Gong, P. Huang, J. Xu, R. Li, S. Yu, X. Cheng, W. Zheng and X. Chen, *Adv. Sci.*, 2020, **7**, 2002210.
34 C. Luo, W. Li, J. Fu and W. Yang, *Chem. Mater.*, 2019, **31**, 5616–5624.
35 Y. Li, C. Wang, G. Xu, G. Luo and Z. Deng, *J. Phys. Chem. Lett.*, 2023, **14**, 2006–2011.
36 X. Yang, C. Pu, H. Qin, S. Liu, Z. Xu and X. Peng, *J. Am. Chem. Soc.*, 2019, **141**, 2288–2298.
37 K. Xing, X. Yuan, Y. Wang, J. Li, Y. Wang, Y. Fan, L. Yuan, K. Li, Z. Wu, H. Li and J. Zhao, *J. Phys. Chem. Lett.*, 2019, **10**, 4177–4184.

